ACS APPLIED MATERIALS & INTERFACES

Research Article

www.acsami.org

Coupled Heterojunction $Sn_2Ta_2O_7$@SnO_2: Cooperative Promotion of Effective Electron−Hole Separation and Superior Visible-light Absorption

Junyu Lang,[†] Congyan Li,[†] Shuwei Wang,[†] Juanjuan Lv,[†] Yiguo Su,[†] Xiaojing Wang,*[,†] and Guangshe Li[‡]

[†]School of Chemistry and Chemical Engineering, Inner Mongolia University, Hohhot City 010021, People's Republic of China

[‡]National Key Laboratory of Inorganic Synthesis and Preparative Chemistry, Chemistry College, Jilin University, Changchun 130023, People's Republic of China

Supporting Information

ABSTRACT: In this work, a novel heterostructure integrated by two wide-band gap semiconductors, SnO_2 and $Sn_2Ta_2O_7$, is successfully prepared via a hydrothermal approach. Hollow $Sn_2Ta_2O_7$ spheres were first formed, and small SnO_2 particles were then well-dispersed onto the outside surface of the spheres, forming a *p*−*n* heterostructure. This heterostructure exhibits a higher potential edge that yielded enhanced photoredox ability. Further, the heterostructure is of Z-type with a consistent internal electric field direction, which effectively separates the photogenerated electron−hole pairs. Although both component semiconductors do not absorb visible light, the resulted *p*−*n* heterostructure is surprisingly observed to show an outstanding photocatalytic performance under visible light illumination. Such a visible light response is concluded to be the consequence of the impurity band formed by Sn^{2+} doped in SnO_2 and Sn^{4+} in $Sn_2Ta_2O_7$ via in situ redox. The existence of coupled Sn^{2+} and Sn^{4+} ions in *p*−*n* heterostructure is responsible for the absence of defects and the regenerated catalytic activities. The findings reported here may provide an approach to fabricate the new types of photocatalysts with a synergetic promotion for visible light absorption and sustained photocatalytic activities by coupling different wide-band semiconductors.

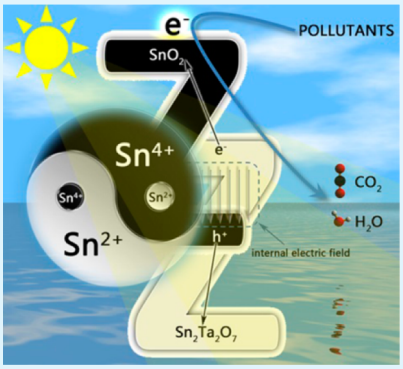

KEYWORDS: *$Sn_2Ta_2O_7$@Sn_2O, heterostructures, visible light, self-doping, photocatalysis*

INTRODUCTION

Photocatalytic technology based on semiconductors has many potential applications in managing environmental pollution and producing clean energy such as hydrogen.[1−3] For a given semiconductor, a larger band gap usually gives rise to a stronger driving force for the photoredox reaction, while a wider band gap would reduce light response range and seriously inhibit solar adsorption. Therefore, enormous efforts have been dedicated to tailoring the electronic structures to make the semiconductor sensitive to visible light without loss of the redox ability.[4−6] It is then well established that the improvement of visible light response of semiconductors can be achieved by introducing intermediate energy levels between conduction band and valence band. In other words, the absorption edge of semiconductors is shifted toward visible light region by doping metals or nonmetal elements into the crystalline lattice.[7−10] Comparing to the conventional doping methods, synthesizing nonstoichiometric metal oxides is more favorable for enhancing visible light absorption while preserving the intrinsic crystal structures of semiconductors without introducing any foreign elements.[11,12] Such a self-doping method has been applied to the preparation of plenty of photocatalytic semiconductors such as reduced TiO_{2-x},[13] Sn^{2+} doped SnO_2,[14−16] C-doped g-C_3N_4,[17] bismuth self-doped Bi_2WO_6,[18] and iodine self-doped $BiOI_x$.[19] However, dopant incorporation would result in an increased amount of defects, which does not favor a higher photocatalytic activity owing to the electron trapping and nonradiative recombination, as demonstrated by both theoretical and experimental studies.[19−22] To promote the redox ability and photocatalytic activity, we extensively studied composite photocatalysts involving two or more components. One type of such composites is usually constructed by coupling semiconductors with larger band gap for the purpose of the higher redox ability, such as WO_3/TiO_2, RuO_2/$NaTaO_3$, and NiO/ZnO.[23−26] The reduction and oxidation reactions could occur at two different potential sites, which effectively inhibit the combination of photoexcited electron−hole pairs. Nevertheless, such composites may fail to secure good visible light response. Another type of composite involves components of narrow band gap semiconductors (e.g., CdS/ZnO,[27] CdS/TiO_2/WO_3,[28] V_2O_5/ZnO,[29] $CuBi_2O_4$/$NaTaO_3$,[30] CuO/$CuWO_4$,[31] SnS_2/SnO_2,[32] and hydrogenated black TiO_2)[33] with an increased visible absorption. Yet, these composites usually suffer from serious

Received: March 26, 2015
Accepted: June 15, 2015
Published: June 15, 2015

DOI: 10.1021/acsami.5b02271
ACS Appl. Mater. Interfaces 2015, 7, 13905−13914

photocorrosion in long-term photocatalytic reaction upon light irradiation. Therefore, it is highly challenging to design a system with a controlled structural arrangement that can efficiently harvest the visible light, meanwhile providing both photoredox power and better stability necessary for energy and environment purposes.

We speculated that if the matched impurity levels can be simultaneously induced in the band gaps for components in wide-band gap semiconductors. Photoredox power and superior visible-light absorption might be cooperatively promoted without loss of the reactive stability. Such a challenging target is highly possible to achieve by integrating two typical wide-gap semiconductors $Sn_2Ta_2O_7$ and SnO_2 with coupled Sn^{2+}−Sn^{4+} ion pairs. This is because (1) $Sn_2Ta_2O_7$ belongs to a class of typical wide-gap semiconductors (4.0 eV) with the merits of very positive electrochemical potential and high chemical stability.[34−38] Once the intrinsic large energy gap could be sufficiently decreased, one may expect tantalates to show visible light response for practical applications; (2) tin ions have variable valence states, and incorporation of tin ions in semiconductors could provide a facile and efficient method to modify the band gaps (like those of SnM_2O_6 and $Sn_2M_2O_7$ (M = Nb or Ta), Sn^{2+}/$KTiNbO_5$, and Sn^{2+}/$K_4Nb_6O_{17}$);[39−42] and (3) when tantalates were hybridized with SnO_2, a common wide-gap photocatalyst (3.6 eV), an in situ redox between both components may occur, which would produce a valence reduction of Sn^{4+} to Sn^{2+} in SnO_2 and, meanwhile, a valence increase from Sn^{2+} to Sn^{4+} in $Sn_2Ta_2O_7$, highly useful for superior visible-light absorption and effective electron−hole separation for enhancing photocatalytic activity of SnO_2.[43,44] Similar cases have been demonstrated in recent studies on other composite materials.[45−50]

In this work, a hollow-sphere p−n heterojunction of $Sn_2Ta_2O_7$@SnO_2 was fabricated by integrating two wide-band semiconductors, SnO_2 and $Sn_2Ta_2O_7$. The combination of electron and holes was restrained by making use of the energy level difference of the coupled species, which increased the catalytic activity. At the same time, the visible light response was derived by simultaneously incorporating Sn^{2+} into SnO_2 and Sn^{4+} into $Sn_2Ta_2O_7$ matrix through in situ redox of tin ions in SnO_2 and $Sn_2Ta_2O_7$, respectively. Eventually, the photocatalytic mechanism was discussed based on the exploration of active species and separation pathway of electron−hole pairs in hollow sphere p−n heterojunction.

EXPERIMENTAL SECTION

Fabrication of Hollow $Sn_2Ta_2O_7$ Spheres. Sample was synthesized via a simple hydrothermal route. First, 2.00 g of tantalum wire (99%) was impregnated into 60 mL hydrofluoric acid aqueous solution (40 wt %), which was then transferred to a Teflon-lined autoclave. The autoclave was sealed and maintained at 80 °C for 48 h. After the solution cooled to room temperature naturally, a hydrosoluble tantalate complex, H_2TaF_7 was obtained. Hydrolysis of H_2TaF_7 with addition of NH_3 (28 wt %) when the pH was close to 8 yielded a white powder as tantalum precursor. Then, the precursor was dried fully at 60 °C for 12 h to remove the raw materials and byproducts (HF, NH_3, H_2O, or NH_4F). This precursor was identified to be in an amorphous state with a nonuniform spherical shape (Figure S1, Supporting Information). Following this procedure, Sn precursor was prepared by hydrolysis of $SnCl_2$ with NaOH (aq), which is determined to be $Sn_6O_4(OH)_4$ by XRD, SEM, and TEM data (Figure S2, Supporting Information). The tantalum precursor was fully mixed with 1.55 g of $Sn_6O_4(OH)_4$ by grinding for 30 min. The molar ratio of Sn to Ta was set at about 1:1. Then, the mixture was added into a Teflon autoclave filled with 60 mL of deionized water. The autoclave was sealed and heated in an oven at 160 °C for 24 h. The final product was dried in an oven at 80 °C after being washed with ethanol and deionized water for 5 times.

Fabrication of $Sn_2Ta_2O_7$@SnO_2. Heterostructure $Sn_2Ta_2O_7$@SnO_2 was prepared by a similar procedure with different molar ratios of Sn to Ta at 1.5:1, 2.0:1, and 2.5:1.

Characterization. Powder X-ray diffraction (XRD) of the as-prepared samples was recorded by a PANalytical Empyrean diffractometer with a copper target. The average grain size, D, was measured from the diffraction peak (110) using Scherrer formula, $D = 0.9\lambda/(\beta\cos\theta)$, where λ is the X-ray wavelength employed, θ is the diffraction angle of the diffraction peak (110), and β is defined as the half width after subtracting the instrumental broadening. Particle sizes and morphologies of the samples were determined using scanning electron microscopy (SEM) on a HITACHI S-4800 apparatus with an acceleration voltage of 20.0 kV and energy dispersive X-ray energy spectroscopy (EDS) was performed at an acceleration voltage of 15 kV. Transmission electron microscopy (TEM), high-resolution transmission electron microscopy (HRTEM) and STEM EDS line scanning profile of the samples were performed using a Tecnai G2 F20 S-TWIN apparatus with an acceleration voltage of 200 kV. UV−vis diffuse-reflectance spectra of the samples were recorded using PerkinElmer UV/VS/NIR Lambda750s spectrometer at room temperature. The specific surface areas of the samples were determined from the nitrogen absorption data at liquid nitrogen temperature using Brunauer−Emmett−Teller (BET) technique on a Micromeritics ASAP 2020 Surface Area and Porosity Analyzer. X-ray photoelectron spectroscopy (XPS) measurements were performed on a Thermo ESCALAB 250 with Al Kα (1486.6 eV) line at 150 W. To compensate surface charges effects, we calibrated the binding energies using C 1s peak at 284.60 eV as the reference. The ^{119}Sn Mössbauer spectrum was recorded under constant geometry with a microprocessor-controlled Mössbauer spectrometer at room temperature using a 5mCi $Ba^{119m}SnO_3$ source. The spectrum was computer-fitted and found to give the most acceptable fits to Lorentzian lines using the MossWinn program . The ^{119}Sn chemical isomer shift data are quoted relative to $BaSnO_3$.

Evaluation of Photocatalytic Activity. A heteropolyaromatic dye, methyl orange (MO), was used as a probe molecule to evaluate the photocatalytic reactivity of the samples. The experiments were carried out at room temperature as follows: 25 mg photocatalyst was dispersed into 50 mL methyl orange (MO) aqueous solution (2.0×10^{-5} M), then the suspension was stirred magnetically for 30 min in the dark to establish an adsorption−desorption equilibrium on the catalyst surface. The suspension was illuminated in a photoreaction apparatus with a 300W Hg lamp with a band-pass filter of 420 nm > λ > 300 nm for UV light and a 400 nm cutoff glass filter for visible light. At given intervals, 5 mL of the suspensions was extracted and subsequently centrifuged. The photocatalytic degradation process was monitored via measuring the absorption of MO at 463 nm with a UV−vis spectrophotometer (UVIKON XL/XS) based on the Lambert−Beer law, where the absorbance at a particular wavelength is proportional to the concentration of MO. To investigate the reactive species, we introduced various scavengers into the MO solution prior to the addition of the photocatalyst. The experimental process was similar to the photodegradation experiment. The dosages of these scavengers were referred to those adopted in previous studies.[51]

Photoelectrochemical Measurements. The Photocurrent experiment was performed using an Autolab model AUT302N.FRA32M.V electrochemical workstation with a three-electrode cell. Ten milligrams (10 mg) of as-prepared sample and 50 μL of nafion solution (5% w/w) were added in 2 mL of ethanol, forming a uniform suspension after 10 min of ultrasonic treatment. The suspension was spin coated on a piece of ITO glass (1 × 1.5 cm) at a speed of 300 rps and then dried at 60 °C for 24 h. Scotch tape (~5 μm thick) has been used as a spacer to fix the film thickness. ITO glass, platinum wire, and Ag/AgCl electrodes were used as working, counter, and reference electrodes, respectively. A 300 W Xe lamp (PLSSXE300, Beijing Trusttech Co. Ltd.) was used as a light source (a UV cutoff filter was equipped to provide visible light ($\lambda \geq 400$ nm)). The electrolyte

DOI: 10.1021/acsami.5b02271
ACS Appl. Mater. Interfaces 2015, 7, 13905−13914

solution was a Na_2SO_4 aqueous solution (0.2 mol L^{-1}). Mott–Schottky plots of $Sn_2Ta_2O_7$@SnO_2 heterostructure was performed at an AC frequency of 10 kHz in the dark.

RESULTS AND DISCUSSION

Fabrication of Hollow $Sn_2Ta_2O_7$ Spheres. Hollow $Sn_2Ta_2O_7$ spheres were fabricated via a simple hydrothermal route. X-ray diffraction pattern of the as-prepared sample was presented in Figure 1a. The XRD peaks appearing at 2θ = 10.5,

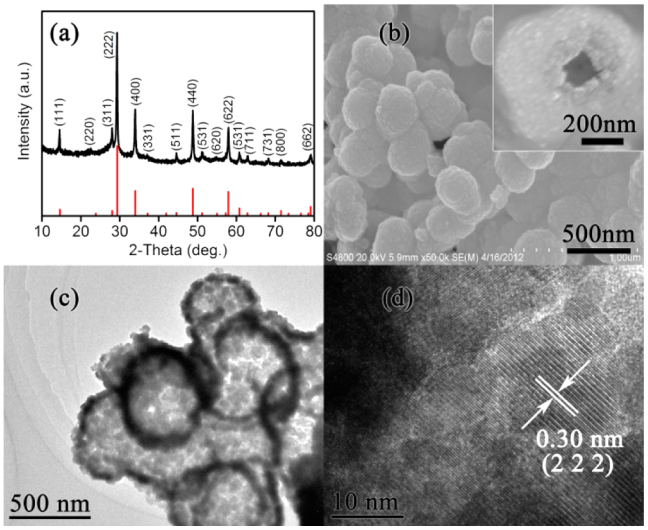

Figure 1. (a) XRD pattern, (b) SEM, (c) TEM, and (d) HR-TEM images of sample $Sn_2Ta_2O_7$. Red vertical bars represent the standard diffraction data for $Sn_2Ta_2O_7$ (JCPDS, No.74-1353). (b, inset) Magnified SEM image of the sample.

20.4, 27.2, 29.8, 34.5, 36.8, 40.0, and 45.6 degrees were ascribed to those of pure phase $Sn_2Ta_2O_7$ of high crystallinity (Joint Committee for Powder Diffractions Standards, JCPDS card No. 74-1353). The crystallinity is high, as indicated by the intense diffractions. The particles of the samples were small, and they piled up and formed a hollow sphere with an average diameter of about 400 nm and a shell thickness of 30–50 nm (Figure 1b and Figure S3, Supporting Information). Moreover, the ring patterns observed by TEM in Figure 1c further confirmed the formation of hollow spheres. As seen from HRTEM images in Figure 1d, the fringe interval is 0.30 nm, which assigned to an interplanar spacing of (222) planes for tetragonal phase $Sn_2Ta_2O_7$, very closely to the value of d = 0.3025 nm for $Sn_2Ta_2O_7$ (222) in JCPDS cards. This conclusion was further confirmed by the data from the energy-dispersive X-ray spectrum (Figure S4, Supporting Information), where $Sn_2Ta_2O_7$ sample was composed of Sn, Ta, and O, and the ratio of Sn/Ta/O was 1:1:3.1, closer to the theoretical ratio of Sn/Ta/O = 1:1:3.5.

Construction of *p–n* Heterojunction of $Sn_2Ta_2O_7$@SnO_2. To prepare the uniform heterostructure of $Sn_2Ta_2O_7$@SnO_2, one-step synthetic route was adopted in this work with a procedure same as that for $Sn_2Ta_2O_7$ except for the molar ratio of Sn to Ta. As illustrated in Figure 2, the key step is to control the molar ratio of Sn to Ta in the raw material. In the presence of a redundant Sn source, the precursor might be easily oxidized to form SnO_2 that was then dispersed onto the outside surface of the preformed hollow $Sn_2Ta_2O_7$ sphere. Such a formation process was further confirmed by treating Ta and Sn-source precursors under similar hydrothermal condition to

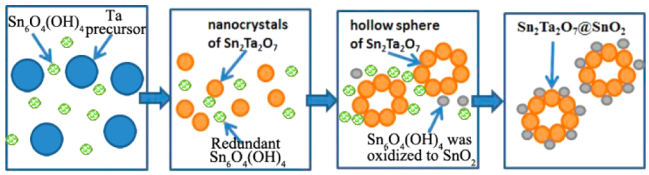

Figure 2. Schematic diagram of the formation processes of heterostructure hollow $Sn_2Ta_2O_7$@SnO_2 spheres: green, blue, orange, and gray balls represent Sn precursor, Ta precursor, $Sn_2Ta_2O_7$, and SnO_2, respectively.

those for preparing composite sample. As shown in Figures S5 and S6 (Supporting Information), for tantalum precursor, the product still kept an amorphous state with partially crystallized $HTaO_3$. Different from tantalum precursor, the product $Sn_6O_4(OH)_4$ was converted to SnO_2, giving evidence of SnO_2 forming by the oxidation of the redundant Sn precursor.

As expected, a composite of $Sn_2Ta_2O_7$@SnO_2 was obtained when the molar ratio of Sn^{2+} to Ta^{5+} was controlled to be larger than 1:1 (Figure 3a). The diffraction peaks of $Sn_2Ta_2O_7$@SnO_2

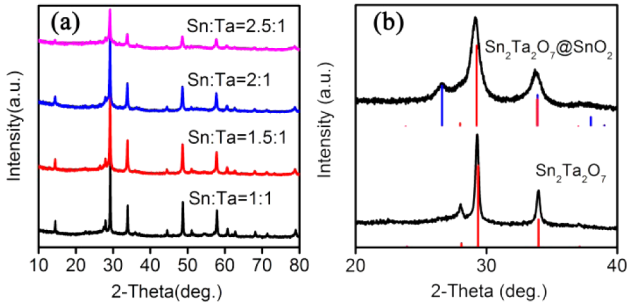

Figure 3. (a) XRD patterns of $Sn_2Ta_2O_7$@SnO_2 at various raw material concentrations, (b) XRD sectional patterns of $Sn_2Ta_2O_7$@SnO_2 and $Sn_2Ta_2O_7$. Red vertical bars represent the standard diffraction data of pure $Sn_2Ta_2O_7$ (JCPDS No.74-1353) and blue vertical bars represent the standard diffraction data of pure SnO_2 (JCPDS No. 71-0652).

were indexed to well-crystallized $Sn_2Ta_2O_7$ and SnO_2 phases (JCPDS No. 74-1353 and 71-0652), respectively. Notably, the crystalline structure did not differ from that of the individual $Sn_2Ta_2O_7$ and SnO_2 except for the broadened peaks (Figure 3b), suggesting that the presence of SnO_2 could inhibit the crystal growth of $Sn_2Ta_2O_7$. Such a morphological construction was confirmed by TEM and SEM images, as shown in Figure 4. For $Sn_2Ta_2O_7$@SnO_2, the well-defined hollow sphere structures were kept except for the rougher surfaces (Figure 4a). Comparing to the pure $Sn_2Ta_2O_7$, TEM rings of the composite sample were small and not very clear, indicating the thickened shells (Figure 4b). As seen from HRTEM images in Figure 4c,d, the fringe interval was 0.34 nm in the region of the tiny particles on the outer surface, which corresponds to the interplanar spacing of (110) for hexagonal phase SnO_2, while that of 0.30 nm corresponds to the interplanar spacing of (222) crystal planes of tetragonal phase $Sn_2Ta_2O_7$ in the shell region. The measurement details are provided in Figure S7 (Supporting Information). To further confirm the formation mechanism proposed for hollow structure $Sn_2Ta_2O_7$@SnO_2, we performed scanning transmission electron microscopy (STEM) (Figure 4e, inset) and energy-dispersive X-ray microanalysis (EDS) line scanning (Figure 4e) along the red arrow direction shown in the inset of Figure 4e. It is noted that the shapes of

DOI: 10.1021/acsami.5b02271
ACS Appl. Mater. Interfaces 2015, 7, 13905–13914

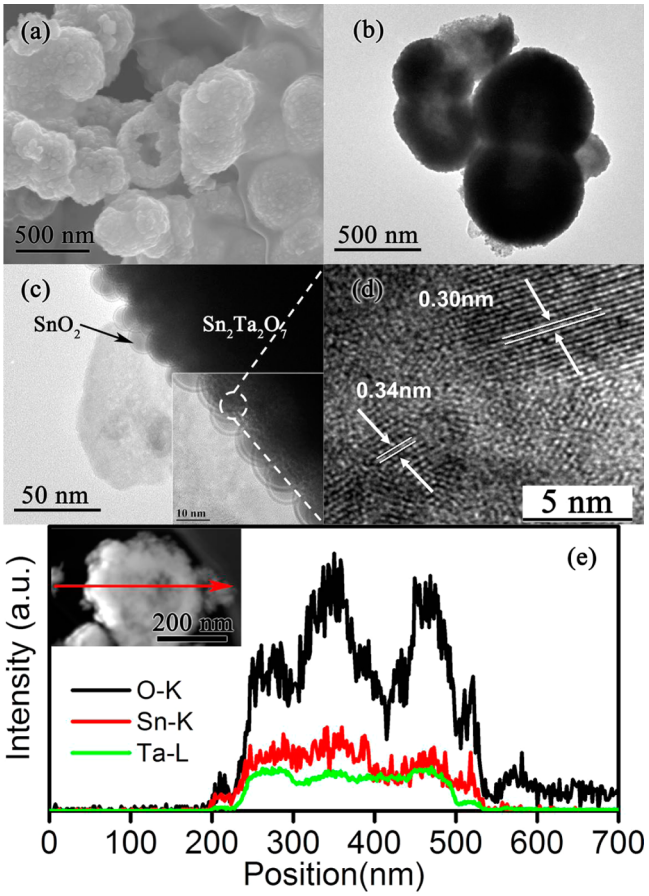

Figure 4. (a) SEM, (b and c) TEM, and (d) HRTEM images of $Sn_2Ta_2O_7$@SnO_2. (e)EDS line scanning profile and (inset) STEM image of a single hollow $Sn_2Ta_2O_7$@SnO_2 sphere. (Recorded through orientation along the red arrow shown in STEM image).

EDS line scans for Sn and Ta were similar and had a flat central region in the position of 215 to 500 nm, giving evidence for hollow sphere structure, as reported elsewhere.[52,53] Moreover, Ta element can be hardly detected in the ranges of 200−215 nm and 505−520 nm. It means that there were only the species composed by Sn and O elements locating on the outer layers of the spherical shell. On the other hand, XPS depth profiling with argon ion etching was performed at different etching periods (Figure S8, Supporting Information). The atomic ratio of Ta to Sn for SnO_2@$Sn_2Ta_2O_7$ was 0.68, which increased to 0.77 after etching for 60s. Therefore, $Sn_2Ta_2O_7$ was probably located in the inner shell of the hollow sphere. Thus, it is concluded that smaller-sized SnO_2 nanoparticles tightly attached to the surface of $Sn_2Ta_2O_7$ nanoparticles in forming the heterostructure hollow spheres. N_2 adsorption−desorption isotherms of $Sn_2Ta_2O_7$@SnO_2 together with $Sn_2Ta_2O_7$ are displayed in Figure S9 (Supporting Information). $Sn_2Ta_2O_7$ exhibited a very small hysteresis loops. Differently, $Sn_2Ta_2O_7$@SnO_2, displayed the type II with a H_3 hysteresis loop according to Brunauer−Deming−Deming−Teller (BDDT) classification. $Sn_2Ta_2O_7$@SnO_2 was characterized to have a mesoporous structure. It is worth noting that BET surface area of $Sn_2Ta_2O_7$@SnO_2 composite was 51 m^2/g, which is smaller than that of $Sn_2Ta_2O_7$ (54 m^2/g).

A careful comparison of XPS spectra for the prepared samples is shown in Figure 5. The peak positions in all of XPS spectra were calibrated with C 1s at 284.60 eV. The survey

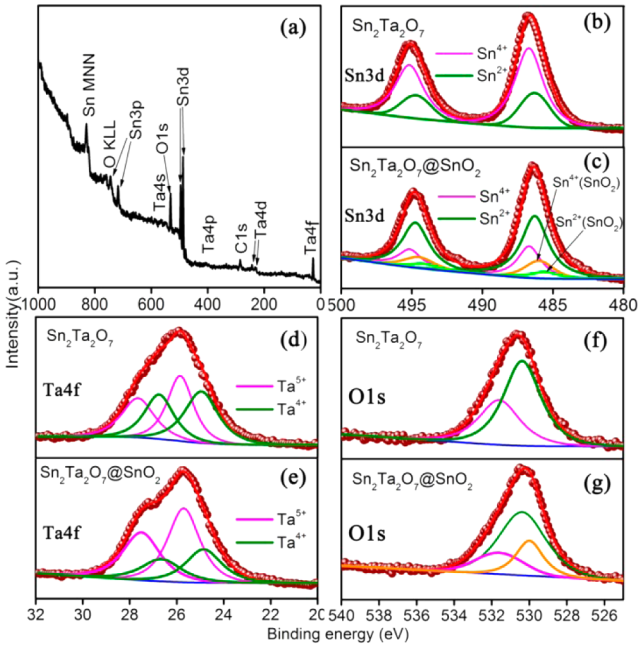

Figure 5. XPS spectra: (a) survey spectrum, (b and c) Sn 3d, (d and e) Ta 4f, and (f and g) O 1s orbital of $Sn_2Ta_2O_7$ and $Sn_2Ta_2O_7$@SnO_2.

spectrum of $Sn_2Ta_2O_7$@SnO_2 in Figure 5a confirmed the presence of Sn, Ta and O elements in the as-prepared samples. The two strong peaks at binding energies around 486 and 495 eV in pure $Sn_2Ta_2O_7$ were fitted into two sets of peaks (Figure 5b). The first set of peaks at 486.7 and 495.2 eV was ascribed to Sn^{4+} ($3d_{5/2}$, $3d_{3/2}$) and the second set of peaks at 486.3 and 494.8 eV was ascribed to Sn^{2+} ($3d_{5/2}$, $3d_{3/2}$). As for $Sn_2Ta_2O_7$@SnO_2, the peaks could be fitted with four sets of peaks, respectively (Figure 5c). The first set and the second set of peaks were completely consistent to that in pure $Sn_2Ta_2O_7$, assigned to the Sn^{4+} ($3d_{5/2}$, $3d_{3/2}$) and Sn^{2+} ($3d_{5/2}$, $3d_{3/2}$) of $Sn_2Ta_2O_7$ in composite $Sn_2Ta_2O_7$@SnO_2. The other two sets of peaks at 486.0, 494.5, 485.6, and 494.1 eV were assigned to Sn^{2+} ($3d_{5/2}$, $3d_{3/2}$) and Sn^{4+} ($3d_{5/2}$, $3d_{3/2}$) of SnO_2 in composite sample, respectively. Thus, it is obviously Sn^{4+} and Sn^{2+} ions were coexisted in $Sn_2Ta_2O_7$ for both pure $Sn_2Ta_2O_7$ and $Sn_2Ta_2O_7$@SnO_2. The same phenomenon appeared for SnO_2 in $Sn_2Ta_2O_7$@SnO_2 composite. The existence of Sn^{4+} in $Sn_2Ta_2O_7$ and Sn^{2+} in SnO_2 matrix was interpreted as self-doping via in situ redox of tin ions. It is proposed that the visible light response might be driven through an impurity band formed by such self-doping.[14] Furthermore, it was observed that the content of Sn^{4+} for $Sn_2Ta_2O_7$ were larger in pure $Sn_2Ta_2O_7$ than that in $Sn_2Ta_2O_7$@SnO_2.[54] As is known, the defects may be caused by unbalanced charges due to the impurity element incorporating crystalline matrix. In terms of our composite sample, a content drop of Sn^{4+} ions meant fewer defects, thus favoring a higher photocatalytic activity owing to the lack of recombination center for electron−hole pairs. XPS signals of Ta 4f for both $Sn_2Ta_2O_7$ and $Sn_2Ta_2O_7$@SnO_2 nanoparticles were fitted to contain two sets of doublets using a series of Lorentzian−Gaussian line shapes according to the references (Figure 5d,e).[48] One set of doublets showed binding energies at 24.9 and 26.7 eV, respectively, which correspond to $4f_{7/2}$ and $4f_{5/2}$ of Ta^{4+}. Another set of doublet with binding energies of 25.7 and 27.5 eV to $4f_{7/2}$ and $4f_{5/2}$ of Ta^{5+}. However, the ratio of Ta^{5+} to Ta^{4+} is different for two

DOI: 10.1021/acsami.5b02271
ACS Appl. Mater. Interfaces 2015, 7, 13905−13914

samples, 1.0 for pure $Sn_2Ta_2O_7$ and 2.0 for $Sn_2Ta_2O_7$@SnO_2. The descending of Ta^{4+} ions in the composite sample compensated for the lack of Sn^{4+} ions that were incorporated into $Sn_2Ta_2O_7$ matrix. The O 1s peaks for $Sn_2Ta_2O_7$@SnO_2 heterostructure (Figure 5f) can be fitted into three peaks at 529.5, 530.6, and 532.2 eV, which correspond to the Ta−O bonds in $[Ta_2O_7]$ slabs of the hollow $Sn_2Ta_2O_7$ sphere structure, Sn−O bonds of SnO_2, and O−H bonds of the surface-adsorbed water, respectively, while for $Sn_2Ta_2O_7$, only two peaks can be assigned to Ta−O bonds in $[Ta_2O_7]$ slabs and the O−H bonds of the surface-adsorbed water, respectively (Figure 5g). The smaller peak area for the surface-adsorbed water in $Sn_2Ta_2O_7$@SnO_2 gave an additional evidence of the fewer defects formed in the surface of the composite. To convince the valences of tin element, we performed ^{119}Sn Mossbauer spectroscopy, and the results are provided in Figure S10 (Supporting Information). It was found a broadened single peak with a zero isomer shift (IS) of δ/$BaSnO_3$, which was assigned to Sn(IV) species. It was concluded these Sn(IV) species should originate from Sn^{4+} in SnO_2 as well as in $Sn_2Ta_2O_7$ due to the same isomer shift as reported in reference.[55,56] A well-resolved doublet with an isomer shift of 2.83 mm/s was assigned Sn(II) species.[57] It could be from Sn^{2+} in SnO_2 and also in $Sn_2Ta_2O_7$. The ratio of Sn(II)/Sn(IV) was about 1:1 in terms of the peaks area and recoilless fractions of Sn^{2+} and Sn^{4+}.[58]

To understand the formation of the heterostructure, we further investigated the inner electronic field and the relative potential edges of $Sn_2Ta_2O_7$@SnO_2. The band energy edges were calculated according to the empirical equations:[4,23]

$$E_{VB} = \chi - E^e + 0.5Eg \quad (1)$$

$$E_{CB} = E_{VB} - E_g \quad (2)$$

where E_{VB} is the valence band edge potential, χ is the electronegativity of the semiconductor, which is the geometric mean of the electronegativity of the constituent atoms, and E^e is the energy of free electrons on the hydrogen scale (about 4.5 eV vs NHE). The E_{VB} values of $Sn_2Ta_2O_7$ and SnO_2 have been estimated to be 2.83 and 3.48 eV vs NHE, and their corresponding E_{CB} are −0.24 and −0.06 eV. Thus, a Z type heterostructure of $Sn_2Ta_2O_7$@SnO_2 was formed, as illustrated in Figure 6.

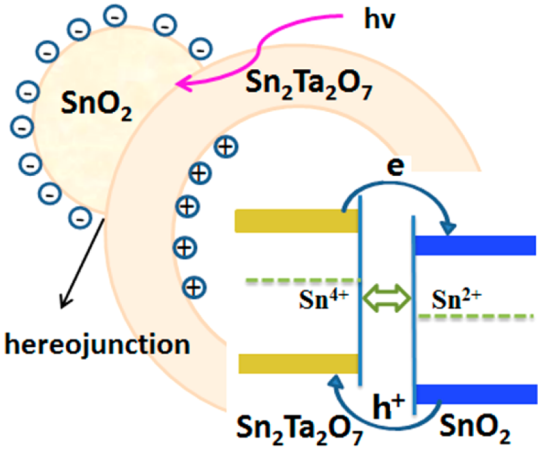

Figure 6. Schematic illustration of the electron-transfer processes on p−n heterojunction $Sn_2Ta_2O_7$@SnO_2.

A p−n junction characteristic was observed in Mott−Schottky plots for the as-prepared sample $Sn_2Ta_2O_7$@SnO_2, where a "V" shape was present due to the coexistence of positive and negative slopes in Figure 7a, as reported

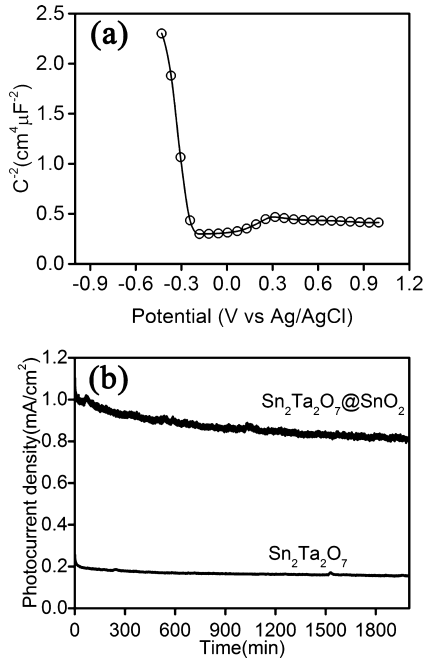

Figure 7. (a) Mott−Schottky plots of $Sn_2Ta_2O_7$@SnO_2 in the dark and (b) time-dependent photocurrent density of the sample $Sn_2Ta_2O_7$ and $Sn_2Ta_2O_7$@SnO_2 under a continuous simulated solar light illumination for 2000s.

elsewhere.[59] Furthermore, $Sn_2Ta_2O_7$ was confirmed to be a n-type semiconductor due to a positive slope of Mott−Schottky plot, as shown in Figure S11 (Supporting Information). Thus, SnO_2 in p−n junction of $Sn_2Ta_2O_7$@SnO_2 would show p-type characteristic. It is well-known that SnO_2 is a typical n-type semiconductor and could be transferred to a p-type when some lower valence ions were incorporated into SnO_2 matrix.[51,53] Thus, it provides additional evidence for the doping of Sn^{2+} in SnO_2 crystalline cell.

When n-type $Sn_2Ta_2O_7$ was in contact with a p-type SnO_2 to form a p−n junction, electrons would diffuse from p-SnO_2 into n-$Sn_2Ta_2O_7$, resulting in an accumulation of negative charges in n-$Sn_2Ta_2O_7$ region near the junction. Meanwhile, holes would diffuse from the n-$Sn_2Ta_2O_7$ region to the p-SnO_2 region, creating a positive section in the p-SnO_2 region in the vicinity of the junction. When the Fermi levels of $Sn_2Ta_2O_7$ and SnO_2 reached equilibration, an internal electric field directed from p-SnO_2 to n-$Sn_2Ta_2O_7$ was simultaneously built to stop the charge diffusion. Meanwhile, the energy bands of SnO_2 shifted downward along with the Fermi level, whereas the energy bands of $Sn_2Ta_2O_7$ shifted upward in this process. Under visible-light irradiation, electron−hole pairs would be photogenerated within $Sn_2Ta_2O_7$. Subsequently, the photogenerated electrons would migrate from $Sn_2Ta_2O_7$ to the CB of SnO_2. However, the VB potential of $Sn_2Ta_2O_7$ is higher than that of SnO_2, so holes can only stay in $Sn_2Ta_2O_7$. It is known that hollow $Sn_2Ta_2O_7$ sphere may provide a shorter pathway and more opportunities for the photogenerated holes to reach the surface of the sphere. Furthermore, the aforementioned internal electric field could promote the separation of the electron−hole

DOI: 10.1021/acsami.5b02271
ACS Appl. Mater. Interfaces 2015, 7, 13905−13914

pairs, causing electrons to move across the interface to the region of SnO_2 and the holes to transfer to the surface. Thus, the reduced recombination probability of photogenerated electron−hole pairs and the enhanced photocatalytic efficiency were expected through an internal electric field due to the presence of potential barrier at $Sn_2Ta_2O_7$@SnO_2 $p-n$ heterostructure interface. The photocurrent shown in Figure 7b was measured by an applied voltage of 0.5 V (vs Ag/AgCl) with light irradiation. As a result, the photocurrent density was greatly enhanced when $Sn_2Ta_2O_7$ was coupled by SnO_2, confirming that the $p-n$ junction facilitated the charge generation and migration, as well as suppressed the charge recombination.

Photocatalytic Properties of Heterojunction $Sn_2Ta_2O_7$@SnO_2. The optical absorption of the as-prepared $Sn_2Ta_2O_7$@SnO_2 was determined by UV−vis diffuse reflectance spectra, and compared with SnO_2 and $Sn_2Ta_2O_7$ (Figure 8). The absorption edges of the three samples were found to be

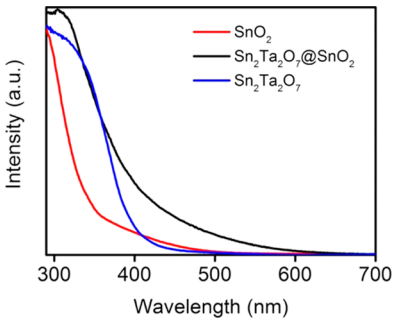

Figure 8. UV−vis absorption spectra of pure $Sn_2Ta_2O_7$, SnO_2, and composite $Sn_2Ta_2O_7$@SnO_2.

around 347 nm for SnO_2, 405 nm for $Sn_2Ta_2O_7$, and 446 nm for the composite $Sn_2Ta_2O_7$@SnO_2. The band gaps calculated were 3.54, 3.06, and 2.73 eV for SnO_2, $Sn_2Ta_2O_7$, and $Sn_2Ta_2O_7$@SnO_2, respectively. Although both SnO_2 and $Sn_2Ta_2O_7$ components are wide band gap semiconductors, the optical absorption of hollow $Sn_2Ta_2O_7$@SnO_2 spheres underwent a large red shift and exhibited an obvious tail absorption in the visible region. This implies that $Sn_2Ta_2O_7$@SnO_2 heterojunction is more efficient in exploiting the sunlight for the photocatalytic purpose.

The photocatalytic activities of the composite $Sn_2Ta_2O_7$@SnO_2 together with the pure SnO_2 and $Sn_2Ta_2O_7$ were investigated by the photocatalytic oxidation of methyl orange (MO). Twenty-five milligrams (25 mg) of the catalysts were suspended in 50 mL of an aqueous solution of 2.0×10^{-5} M MO. The adsorption efficiency was first evaluated with the adsorption of MO onto the as-prepared photocatalyst as a function of contact time (IS, Figure S12, Supporting Information). Adsorption of MO onto photocatalyst can be ignored because MO nearly did not adsorb onto the samples until irradiation for 100 min. Figure 9 shows the degradation curves of MO at the presence of SnO_2, $Sn_2Ta_2O_7$, and $Sn_2Ta_2O_7$@SnO_2 heterostructure under UV with a band-pass filter of 420 nm > λ > 300 nm and visible (λ > 400 nm) light irradiation. C_0 and C are the concentrations of MO aqueous solution at the irradiation times of 0 (i.e., after the dark adsorption equilibrium) and t min, respectively. In both Figure 9, the blank test shows that the concentration of MO was nearly invariable after UV or visible light irradiation, indicating

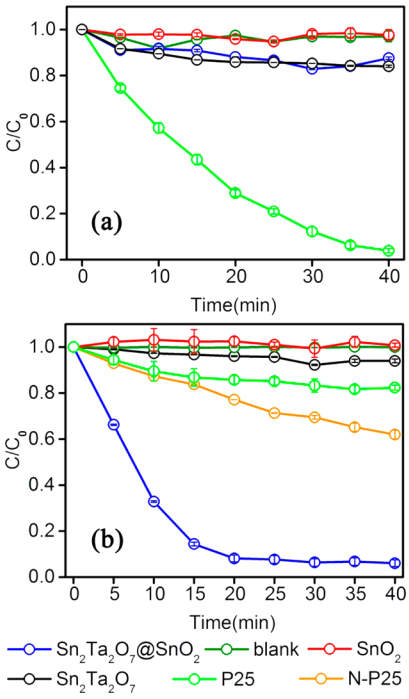

Figure 9. Degradation of methyl orange under (a) UV with a band-pass filter of 420 nm > λ > 300 nm and (b) visible light (λ > 400 nm) irradiation. The light intensity was 6.82 mW/cm^2 and 3.45 mW/cm^2, respectively.

that the self-decomposition can be ignored during the photocatalysis caused by catalyst particles. Meanwhile, less degradation of MO occurred in the presence of only SnO_2 or $Sn_2Ta_2O_7$ nanoparticles. As observed in Figure 9a, degradation efficiency of MO was determined to be about 99% for P25 and 12.5% for $Sn_2Ta_2O_7$@SnO_2 under UV irradiation (420 nm > λ > 300 nm) for 40 min. Because P25 has no activity under visible light, for the purpose of comparison, N-doped P25 was synthesized in terms of the procedure in literature.[22] Remarkably, $Sn_2Ta_2O_7$@SnO_2 composite showed an enhanced activity under visible light with 98.4% degradation efficiency after illumination for 20 min (Figure 9b). However, under the same conditions, the degradation efficiency of MO for N-doped P25 can reach up to 38.1%, while for P25 it was only 16.8% after illuminating 20 min. Further contrast experiment results were shown in Figure S13 (Supporting Information) under visible light conditions using the photocatalyst Sn^{2+} doped $ZnWO_4$ previously reported by our lab and self-doped SnO_2 synthesized according to the reports in references.[9,14,32] It is found that the self-doped SnO_2 needs double the time to completely degrade MO compared to our composite sample, although it showed well visible-light photocatalytic activity.

The photodegradation of MO can be considered as a pseudo-first-order reaction, and the reaction rate was expressed as follows:

$$-\ln(C/C_0) = kt \quad (3)$$

where k is the observed pseudo-first-order reaction rate constant. By plotting $-\ln(C/C_0)$ as a linear function of irradiation time in Figure S14 (Supporting Information), the rate constant k that is the slope of the line can be determined for each photocatalytic reaction (Table 1). The value of k for $Sn_2Ta_2O_7$@SnO_2 sample was 0.131 min^{-1}, about 28 times larger than that of P25 and 11 times larger than that of the N-

DOI: 10.1021/acsami.5b02271
ACS Appl. Mater. Interfaces 2015, 7, 13905−13914

Table 1. Obtained k from the Fitted Linear Plot of $\ln(C/C_0)$ vs t

samples	rate constant, $k \times 10^{-3}$ (min^{-1})	
	UV	visible
$Sn_2Ta_2O_7$@SnO_2	2.61 ± 0.58	131.12 ± 7.71
$Sn_2Ta_2O_7$	1.28 ± 0.33	1.75 ± 0.28
SnO_2	0.04 ± 0.33	0 ± 0.69
N−P25		11.99 ± 0.36
P25	80.61 ± 5.27	4.58 ± 0.67

P25 under visible-light irradiation. Further, the observed photocatalytic performance is far better than most of the reported photocatalysts which has been presented in Table S1 (Supporting Information). To measure the performance of photocatalysts in photodegradation process, we calculated the apparent quantum efficiency (Table S2, Supporting Information). Under visible-light irradiation, it was 6.366×10^{-7} mmol·min^{-1}·mW^{-1} for $Sn_2Ta_2O_7$@SnO_2, larger than those for single components (e.g., 0.243×10^{-7} mmol·min^{-1}·mW^{-1} for $Sn_2Ta_2O_7$ and 0.097×10^{-7} mmol·min^{-1}·mW^{-1} for SnO_2) or that of 5.348×10^{-7}. mmol·min^{-1}·mW^{-1} for self-doped SnO_2.

Such synergistic improvement in visible-light absorption and photocatalytic properties of the composite $Sn_2Ta_2O_7$@SnO_2 may be ascribed to an integration of SnO_2 and $Sn_2Ta_2O_7$ components into a $p-n$ heterostructure. Generally, photocatalysis involves the generation of electrons in the conduction band and holes in the valence band within a semiconductor upon light irradiation at energies equal to or greater than the band gap. In the Z type heterostructure of $Sn_2Ta_2O_7$@SnO_2 as illustrated in Figure 6, it can be concluded that electrons were accumulated in SnO_2 nanoparticles. Basically, the main carriers on the surface can be confirmed by detecting the active species in the reactive systems. Two milliliters (2 mL) of the different captures was added to the solution of MO. Figure 10a indicates the time courses of MO photodegradation by our catalysts under different additive agents. It was found that the degradation efficiency did not change by the addition of *tert*-butyl alcohol (TBA), an excellent capturer of ·OH. Furthermore, the degradation of MO was reduced to 75% when 0.1 g of ammonium oxalate (AO) was added to the reaction systems. We know that holes could be captured by AO; however, with the addition of $AgNO_3$ or benzoquinone, the effective capturers of electrons, we found almost no degradation of MO. Thus, it is concluded that electron and $O_2^{\bullet-}$ maybe the main reactive species in the system. Further evidence comes from the determination of the negative zeta potential, where a large negative value of −50.4 mV was obtained, which confirmed a negative nature because a surface Sn^{4+} ions easily loses two positive charges to convert itself into Sn^{2+}. Thus, it is proposed that a highly photocatalytic efficiency is attributed to the reduced recombination probability of photogenerated electrons and holes through an internal electric field due to the presence of potential barrier at $Sn_2Ta_2O_7$@SnO_2 heterostructure interface. More reactive sites for the photogenerated charger carriers as provided by these hollow spheres produce positive effects on photocatalysis performance.

Enhancement in the visible region could be attributed to the possible mutual diffusion of Sn^{2+} and Sn^{4+} in heterostructure along a local internal electric field on the interface. The process can be described as self-doping via in situ redox, which may result in the formation of impurity band in SnO_2 as well as $Sn_2Ta_2O_7$. In references for SnO_2,[43,44] the visible activity has been caused by the impurity band of Sn^{2+}, consistent with our results. Surely, this self−doping is easier and more effective than the general doping process, which has to consider the crystal energy, charge matching, and compatibility of ions radius due to the introduction of foreign ions. More importantly, the existence of coupled Sn^{2+} and Sn^{4+} ions always retains the charge balance in the materials. Thus, the cation vacancy could be greatly reduced, which usually act as the combination centers of electron−hole pairs for the decrease of catalytic activities. Actually, XPS signals of Ta 4f confirmed the absence of the cation vacancies in our heterostructure samples (Figure 5d,e). Figure 10b shows the photocurrent−voltage curves for $Sn_2Ta_2O_7$@SnO_2 and $Sn_2Ta_2O_7$ under several on/off visible-light irradiation cycles. Both samples were prompt in generating photocurrent with a reproducible response and recover rapidly in the dark to on/off cycles. It is found that the photocurrent density response of as-prepared $Sn_2Ta_2O_7$@SnO_2 was reversible and stable, implying that the current can reproducibly increase violently under each irradiation and recover rapidly in the dark. In comparison with pure $Sn_2Ta_2O_7$, $Sn_2Ta_2O_7$@SnO_2 exhibited an obviously larger photocurrent under each visible light irradiation ($\lambda > 400$ nm). The photocurrent conversion efficiency of $Sn_2Ta_2O_7$@SnO_2 was about 5 times higher than that of $Sn_2Ta_2O_7$. Higher photocurrent means lower recombination of electron−hole pairs, recoverable photoelectron emigration, and more visible light absorption, which will eventually contribute to the enhanced photocatalytic activity. Importantly, semiconductor photocatalysis is based on a series of reductive and oxidative reactions which occur on the photon activated surface of catalyst. To some extent, higher photocurrent also displays an improved redox property or photocatalytic activity of the various samples. In addition, the Sn^{2+} and Sn^{4+} contents of $Sn_2Ta_2O_7$@SnO_2 before photocatalytic degradation and after three cycles experiments (Figure S15, Supporting Information)

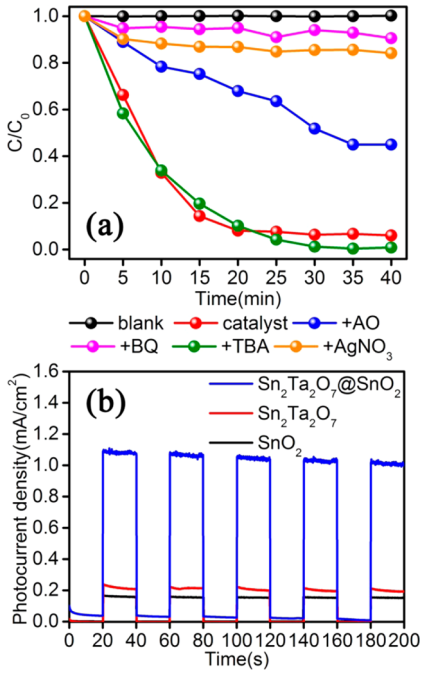

Figure 10. (a) Photocatalytic degradation of MO over $Sn_2Ta_2O_7$@SnO_2 in different inhibitor under visible light irradiation (>400 nm). (b) Photocurrents of $Sn_2Ta_2O_7$@SnO_2, $Sn_2Ta_2O_7$, and SnO_2 under the irradiation of visible light. The light intensity was 3.45 mW/cm^2.

DOI: 10.1021/acsami.5b02271
ACS Appl. Mater. Interfaces 2015, 7, 13905−13914

were determined by XPS spectra of Sn 3d 2/5. The results were shown in Figure S16 (Supporting Information). It is found that the contents of Sn^{2+} and Sn^{4+} ions were substantially unchanged in $Sn_2Ta_2O_7$ with only a slight decrease of Sn^{2+} content in SnO_2. This gave further confirmation of the sample stability. The observed stability and enhanced photocurrents for $Sn_2Ta_2O_7$@SnO_2 have clearly demonstrated the advantages of the highly improved photocatalytic activity.

CONCLUSIONS

A novel *p*−*n* heterostructure $Sn_2Ta_2O_7$@SnO_2 with a coupled Sn^{2+}-Sn^{4+} pair was fabricated via a simple hydrothermal approach. The systematic sample characterization of XRD, XPS, TEM and SEM indicated the coexistence of SnO_2 and $Sn_2Ta_2O_7$ in the $Sn_2Ta_2O_7$@SnO_2 heterostructure by means of the small SnO_2 particles being attached onto the outside surfaces of hollow $Sn_2Ta_2O_7$ sphere. The UV experiment revealed that hollow $Sn_2Ta_2O_7$@SnO_2 spheres underwent a large red shift and exhibited an obvious tail absorption in the visible region, although both SnO_2 and $Sn_2Ta_2O_7$ are wide band gap semicondutors. The as-prepared composites displayed a high photocatalytic activity under visible light irradiation compared to bare SnO_2 or $Sn_2Ta_2O_7$. Specially, the degradation of methyl orange reached up to 98.4% after illumination for 20 min with visible light for $Sn_2Ta_2O_7$@SnO_2 heterostructures, much higher than that of the commercial N-doped P25 with only 38.1% degradation efficiency under the same conditions. The enhanced photoredox ability was attributed to the higher potential edges and the Z-type heterostructure of $Sn_2Ta_2O_7$@SnO_2 which can effectively separate the photogenerated electron−hole pairs. The impurity bands formed in SnO_2 and $Sn_2Ta_2O_7$, originating from the mutual diffusion of Sn^{2+} and Sn^{4+} ions along with a local internal electric field on the interface, led to the absence of cation vacancy and superior visible light absorption. The quenching effects of different scavengers suggested that the reactive photogenerated electron and $O_2^{\bullet-}$ played the major role in the MO degradation. The present work may be applicable to fabricate new types of photocatalysts with a synergetic promotion for visible-light absorption and sustained photocatalytic activities by coupling semiconductors of wide band gaps.

ASSOCIATED CONTENT

Supporting Information

Additional tables and figures as noted in text. The Supporting Information is available free of charge on the ACS Publications website at DOI: 10.1021/acsami.5b02271.

AUTHOR INFORMATION

Corresponding Author

*Fax:+86-471-4992981. Tel:+86-471-4344579. E-mail: wang_xiao_jing@hotmail.com.

Notes

The authors declare no competing financial interest.

ACKNOWLEDGMENTS

This work was financially supported by National Natural Science Foundation of China (Grants 21103081 and 21267014) and the Project of Scientific and Technological Innovation Team of Inner Mongolia University (12110614).

REFERENCES

(1) Zhu, J. F.; Zach, M. Nanostructured Materials for Photocatalytic Hydrogen Production. *Curr. Opin. Colloid Interface Sci.* **2009**, *14*, 260−269.

(2) Fujishima, A.; Zhang, X.; Tryk, D. A. Heterogeneous Photocatalysis: From Water Photolysis to Applications in Environmental Cleanup. *Int. J. Hydrogen Energy* **2007**, *32*, 2664−2672.

(3) de Richter, R.; Caillol, S. Fighting Global Warming: The Potential of Photocatalysis Against CO_2, CH_4, N_2O, CFCs, Tropospheric O_3, BC, and other Major Contributors to Climate Change. *J. Photochem. Photobiol., C* **2011**, *12*, 1−19.

(4) Gao, C.; Li, J. T.; Shan, Z. C.; Huang, F. G.; Shen, H. L. Preparation and Visible-Light Photocatalytic Activity of In_2S_3/TiO_2 Composite. *Mater. Chem. Phys.* **2010**, *122*, 183−187.

(5) Yang, X. F.; Cui, H. Y.; Li, Y.; Qin, J. L.; Zhang, R. X.; Tang, H. Fabrication of Ag_3PO_4-Graphene Composites with Highly Efficient and Stable Visible Light Photocatalytic Performance. *ACS Catal.* **2013**, *3*, 363−369.

(6) Xiong, P.; Zhu, J. W.; Wang, X. Cadmium Sulfide-Ferrite Nanocomposite as a Magnetically Recyclable Photocatalyst with Enhanced Visible-Light-Driven Photocatalytic Activity and Photostability. *Ind. Eng. Chem. Res.* **2013**, *52*, 17126−17133.

(7) Tian, N.; Zhang, Y. H.; Huang, H. W.; He, Y.; Guo, Y. X. Influences of Gd Substitution on the Crystal Structure and Visible-Light-Driven Photocatalytic Performance of Bi_2WO_6. *J. Phys. Chem. C* **2014**, *118*, 15640−15648.

(8) Su, Y.; Lang, J. Y.; Li, L. P.; Guan, K.; Du, C. F.; Peng, L. M.; Han, D.; Wang, X. J. Unexpected Catalytic Performance in Silent Tantalum Oxide through Nitridation and Defect Chemistry. *J. Am. Chem. Soc.* **2013**, *135*, 11433−11436.

(9) Su, Y. G.; Zhu, B. L.; Guan, K.; Gao, S. S.; Lv, L.; Du, C. F.; Peng, L. M.; Hou, L. C.; Wang, X. J. Particle Size and Structural Control of $ZnWO_4$ Nanocrystals via Sn^{2+} Doping for Tunable Optical and Visible Photocatalytic Properties. *J. Phys. Chem. C* **2012**, *116*, 18508−18517.

(10) Su, Y. G.; Wang, S. W.; Meng, Y.; Han, H.; Wang, X. J. Dual Substitutions of Single Dopant Cr^{3+} in Perovskite $NaTaO_3$: synthesis, Structure, and Photocatalytic Performance. *RSC Adv.* **2012**, *2*, 12932−12939.

(11) Lounis, S. D.; Runnerstrorm, E. L.; Llordes, A.; Milliron, D. J. Defect Chemistry and Plasmon Physics of Colloidal Metal Oxide Nanocrystals. *J. Phys. Chem. Lett.* **2014**, *5*, 1564−1574.

(12) Shi, Y. Z.; Ndione, P. F.; Lim, L. Y.; Sokaras, D.; Weng, T. C.; Nagaraja, A. R.; Karydas, A. G.; Perkins, J. D.; Mason, T. O.; Ginley, D. S.; Zunger, A.; Toney, M. F. Self-Doping and Electrical Conductivity in Spinel Oxides: Experimental Validation of Doping Rules. *Chem. Mater.* **2014**, *26*, 1867−1873.

(13) Zhu, Q.; Peng, Y.; Lin, L.; Fan, C. M.; Gao, G. Q.; Wang, R. X.; Xu, A. W. Stable Blue TiO_{2-x} Nanoparticles for Efficient Visible Light Photocatalysts. *J. Mater. Chem. A* **2014**, *2*, 4429−4437.

(14) Long, J. L.; Xue, W. W.; Xie, X. Q.; Gu, Q.; Zhou, Y. G.; Chi, Y. W.; Chen, W. K.; Ding, Z. X.; Wang, X. X. Sn^{2+} Dopant Induced Visible-Light Activity of SnO_2 Nanoparticles for H_2 Production. *Catal. Commun.* **2011**, *16*, 215−219.

(15) Wang, H. K.; Rogach, A. L. Hierarchical SnO_2 Nanostructures: Recent Advances in Design, Synthesis, and Applications. *Chem. Mater.* **2014**, *26*, 123−133.

(16) Fan, C. M.; Peng, Y.; Zhu, Q.; Lin, L.; Wang, R. X.; Xu, A. W. Synproportionation Reaction for the Fabrication of Sn^{2+} Self-Doped SnO_{2-x} Nanocrystals with Tunable Band Structure and Highly Efficient Visible Light Photocatalytic Activity. *J. Phys. Chem. C* **2013**, *117*, 24157−24166.

(17) Dong, G. H.; Zhao, K.; Zhang, L. Z. Carbon Self-Doping Induced High Electronic Conductivity and Photoreactivity of g-C_3N_4. *Chem. Commun.* **2012**, *48*, 6178−6180.

(18) Ding, X.; Zhao, K.; Zhang, L. Z. Enhanced Photocatalytic Removal of Sodium Pentachlorophenate with Self-Doped Bi_2WO_6 under Visible Light by Generating More Superoxide Ions. *Environ. Sci. Technol.* **2014**, *48*, 5823−5831.

DOI: 10.1021/acsami.5b02271
ACS Appl. Mater. Interfaces 2015, 7, 13905−13914

(19) Zhang, X.; Zhang, L. Z. Electronic and Band Structure Tuning of Ternary Semiconductor Photocatalysts by Self Doping: The Case of BiOI. *J. Phys. Chem. C* **2010**, *114*, 18198−18206.
(20) Devi, L. G.; Kottam, N.; Murthy, B. N.; Kumar, S. G. Enhanced Photocatalytic Activity of Transition Metal Ions Mn^{2+}, Ni^{2+}, and Zn^{2+} Doped Polycrystalline Titania for the Degradation of Aniline Blue under UV/Solar Light. *J. Mol. Catal. A: Chem.* **2010**, *328*, 44−52.
(21) Thompson, T. L.; Yates, J. T. Surface Science Studies of the Photoactivation of TiO_2—New Photochemical Processes. *Chem. Rev.* **2006**, *106*, 4428−4453.
(22) Asahi, R.; Morikawa, T.; Ohwaki, T.; Aoki, K.; Taga, Y. Visible-Light Photocatalysis in Nitrogen-Doped Titanium Oxides. *Science* **2001**, *293*, 269−271.
(23) Xiao, F. X. Construction of Highly Ordered ZnO−TiO_2 Nanotube Arrays (ZnO/TNTs) Heterostructure for Photocatalytic Application. *ACS Appl. Mater. Interfaces* **2012**, *4*, 7054−7062.
(24) Torres-Martinez, L. M.; Gomez, R.; Vazquez-Cuchillo, O.; Juarez-Ramirez, I.; Cruz-Lopez, A.; Alejandre-Sandoval, F. J. Enhanced Photocatalytic Water Splitting Hydrogen Production on RuO_2/La $NaTaO_3$ Prepared by Sol−Gel Method. *Catal. Commun.* **2010**, *12*, 268−272.
(25) Song, K. Y.; Park, M. K.; Kwon, Y. T.; Lee, H. W.; Chung, W. J.; Lee, W. I. Preparation of Transparent Particulate MoO_3/TiO_2 and WO_3/TiO_2 Films and Their Photocatalytic Properties. *Chem. Mater.* **2001**, *13*, 2349−2355.
(26) Zhang, Z. Y.; Shao, C. L.; Li, X. H.; Wang, C. H.; Zhang, M. Y.; Liu, Y. C., Electrospun Nanofibers of *p*-Type NiO/*n*-Type ZnO Heterojunctions with Enhanced Photocatalytic Activity. *ACS Appl. Mater. Interfaces*, *2*, 2915−2923.
(27) Barpuzary, D.; Khan, Z.; Vinothkumar, N.; De, M.; Qureshi, M. Hierarchically Grown Urchinlike CdS@ZnO and CdS@Al_2O_3 Heteroarrays for Efficient Visible-Light-Driven Photocatalytic Hydrogen Generation. *J. Phys. Chem. C* **2012**, *116*, 150−156.
(28) Kim, H. I.; Kim, J.; Kim, W.; Choi, W. Enhanced Photocatalytic and Photoelectrochemical Activity in the Ternary Hybrid of CdS/TiO_2/WO_3 through the Cascadal Electron Transfer. *J. Phys. Chem. C* **2011**, *115*, 9797−9805.
(29) Zou, C. W.; Rao, Y. F.; Alyamani, A.; Chu, W.; Chen, M. J.; Patterson, D. A.; Emanuelsson, E. A. C.; Gao, W. Heterogeneous Lollipop-like V_2O_5/ZnO Array: A Promising Composite Nanostructure for Visible Light Photocatalysis. *Langmuir* **2010**, *26*, 11615−11620.
(30) Deng, Y. Y.; Chen, Y. J.; Chen, B. G.; Ma, J. H. Preparation, Characterization and Photocatalytic Activity of $CuBi_2O_4/NaTaO_3$ Coupled Photocatalysts. *J. Alloys Compd.* **2013**, *559*, 116−122.
(31) Chen, H. H.; Leng, W. H.; Xu, Y. M. Enhanced Visible-Light Photoactivity of $CuWO_4$ through a Surface-Deposited CuO. *J. Phys. Chem. C* **2014**, *118*, 9982−9989.
(32) Zhang, Y. C.; Du, Z. N.; Li, K. W.; Zhang, M.; Dionysiou, D. D. High-Performance Visible-Light-Driven SnS_2/SnO_2 Nanocomposite Photocatalyst Prepared via In situ Hydrothermal Oxidation of SnS_2 Nanoparticles. *ACS Appl. Mater. Interfaces* **2011**, *3*, 1528−1537.
(33) Hu, Y. H. A Highly Efficient Photocatalyst—Hydrogenated Black TiO_2 for the Photocatalytic Splitting of Water. *Angew. Chem., Int. Ed.* **2012**, *51*, 12410−12412.
(34) Kato, H.; Asakura, K.; Kudo, A. Highly Efficient Water Splitting into H_2 and O_2 over Lanthanum-Doped $NaTaO_3$ Photocatalysts with High Crystallinity and Surface Nanostructure. *J. Am. Chem. Soc.* **2003**, *125*, 3082−3089.
(35) Zhou, C.; Chen, G.; Li, Y. X.; Zhang, H. J.; Pei, J. A. Photocatalytic Activities of $Sr_2Ta_2O_7$ Nanosheets Synthesized by a Hydrothermal Method. *Int. J. Hydrogen Energy* **2009**, *34*, 2113−2120.
(36) Shi, R.; Lin, J.; Wang, Y. J.; Xu, J.; Zhu, Y. F. Visible-Light Photocatalytic Degradation of $BiTaO_4$ Photocatalyst and Mechanism of Photocorrosion Suppression. *J. Phys. Chem. C* **2010**, *114*, 6472−6477.
(37) Kudo, A.; Kato, H.; Nakagawa, S. Water Splitting into H_2 and O_2 on New $Sr_2M_2O_7$ (M = Nb and Ta) Photocatalysts with Layered Perovskite Structures: Factors Affecting the Photocatalytic Activity. *J. Phys. Chem. B* **2000**, *104*, 571−575.
(38) Yang, M.; Huang, X. L.; Yan, S. C.; Li, Z. S.; Yu, T.; Zou, Z. G. Improved Hydrogen Evolution Activities under Visible Light Irradiation over $NaTaO_3$ Codoped with Lanthanum and Chromium. *Mater. Chem. Phys.* **2010**, *121*, 506−510.
(39) Boppana, V. B. R.; Lobo, R. F. SnO_x−$ZnGa_2O_4$ Photocatalysts with Enhanced Visible Light Activity. *Acs Catal.* **2011**, *1*, 923−928.
(40) Hosogi, Y.; Shimodaira, Y.; Kato, H.; Kobayashi, H.; Kudo, A. Role of Sn^{2+} in the Band Structure of SnM_2O_6 and $Sn_2M_2O_7$ (M = Nb and Ta) and their Photocatalytic Properties. *Chem. Mater.* **2008**, *20*, 1299−1307.
(41) Li, Q. Y.; Kako, T.; Ye, J. H. Facile Ion-Exchanged Synthesis of Sn^{2+} Incorporated Potassium Titanate Nanoribbons and their Visible-Light-Responded Photocatalytic Activity. *Int. J. Hydrogen Energy* **2011**, *36*, 4716−4723.
(42) Trotochaud, L.; Boettcher, S. W. Synthesis of Rutile-Phase $Sn_xTi_{1-x}O_2$ Solid-Solution and $(SnO_2)_x/(TiO_2)_{1-x}$ Core/Shell Nanoparticles with Tunable Lattice Constants and Controlled Morphologies. *Chem. Mater.* **2011**, *23*, 4920−4930.
(43) Osterloh, F. E. Inorganic Materials as Catalysts for Photochemical Splitting of Water. *Chem. Mater.* **2008**, *20*, 35−54.
(44) Wang, N.; Xu, J. X.; Guan, L. H. Synthesis and Enhanced Photocatalytic Activity of Tin Oxide Nanoparticles Coated on Multi-Walled Carbon Nanotube. *Mater. Res. Bull.* **2011**, *46*, 1372−1376.
(45) Wu, S. S.; Cao, H. Q.; Yin, S. F.; Liu, X. W.; Zhang, X. R. Amino Acid-Assisted Hydrothermal Synthesis and Photocatalysis of SnO_2 Nanocrystals. *J. Phys. Chem. C* **2009**, *113*, 17893−17898.
(46) Zeng, J.; Wang, H.; Zhang, Y. C.; Zhu, M. K.; Yan, H. Hydrothermal Synthesis and Photocatalytic Properties of Pyrochlore $La_2Sn_2O_7$ Nanocubes. *J. Phys. Chem. C* **2007**, *111*, 11879−11887.
(47) Fujishima, M.; Jin, Q. L.; Yamamoto, H.; Tada, H.; Nolan, M. Tin Oxide-Surface Modified Anatase Titanium(IV) Dioxide with Enhanced UV-light Photocatalytic Activity. *Phys. Chem. Chem. Phys.* **2012**, *14*, 705−711.
(48) Wen, Z. H.; Wang, G.; Lu, W.; Wang, Q.; Zhang, Q.; Li, J. H. Enhanced Photocatalytic Properties of Mesoporous SnO_2 Induced by Low Concentration ZnO Doping. *Cryst. Growth Des.* **2007**, *7*, 1722−1725.
(49) Niu, M. T.; Huang, F.; Cui, L. F.; Huang, P.; Yu, Y. L.; Wang, Y. S. Hydrothermal Synthesis, Structural Characteristics, and Enhanced Photocatalysis of SnO_2/α-Fe_2O_3 Semiconductor Nanoheterostructures. *ACS Nano* **2010**, *4*, 681−688.
(50) Vinodgopal, K.; Kamat, P. V. Enhanced Rates of Photocatalytic Degradation of an Azo Dye Using SnO_2/TiO_2 Coupled Semiconductor Thin Films. *Environ. Sci. Technol.* **1995**, *29*, 841−845.
(51) Kumar, V.; Govind; Uma, S. Investigation of Cation (Sn^{2+}) and Anion (N^{3-}) Substitution in favor of Visible Light Photocatalytic Activity in the Layered Perovskite $K_2La_2Ti_3O_{10}$. *J. Hazard. Mater.* **2011**, *189*, 502−508.
(52) Mondi, C.; Leifer, K.; Mavrocordatos, D.; Perret, D. Analytical Electron Microscopy As a Tool for Accessing Colloid Formation Process in Natural Waters. *J. Microsc.* **2002**, *207*, 180−190.
(53) Wu, J.; Peng, Z.; Yang, H. Supportless Oxygen Reduction Electrocatalysts of CoCuPt Hollow Nanoparticles. *Philos. Trans. R. Soc., A* **2010**, *368*, 4261−4274.
(54) Stewart, D. J.; Knop, O.; Meads, R. E.; Parker, W. G. Pyrochlores. IX. Partially Oxidized $Sn_2Nb_2O_7$ and $Sn_2Ta_2O_7$: A Mössbauer Study of Sn(II,IV) Compounds. *Can. J. Chem.* **1973**, *51*, 1041−1049.
(55) Lippens, P. E. Interpretation of the ^{119}Sn Mössbauer Isomer Shifts in Complex Tin Chalcogenides. *Phys. Rev. B* **1999**, *60*, 4576−4586.
(56) Nayral, C.; Viala, E.; Fau, P.; Senocq, F.; Jumas, J.-C.; Maisonnat, A.; Chaudret, B. Synthesis of Tin and Tin Oxide Nanoparticles of Low Size Dispersity for Application in Gas Sensing. *Chem.—Eur. J.* **2000**, *6*, 4082−4090.

DOI: 10.1021/acsami.5b02271
ACS Appl. Mater. Interfaces 2015, 7, 13905−13914

(57) David, J. S.; Osvald, K. Pyrochlores. IX. Partially Oxidized $Sn_2Nb_2O_7$, and $Sn_2Ta_2O_7$: A Mössbauer Study of Sn(II,IV) Compounds. *Can. J. Chem.* **1973**, *51*, 1041−1049.
(58) Conte, D. E.; Aboulaich, A.; Robert, F.; Olivier-Fourcade, J.; Jumas, J.-C.; Jordy, C.; Willmann, P. $Sn_x[BPO_4]_{1-x}$ Composites as Negative Electrodes for Lithium Ion Cells: Comparison with Amorphous $SnB_{0.6}P_{0.4}O_{2.9}$ and Effect of Composition. *J. Solid State Chem.* **2010**, *183*, 65−75.
(59) Li, J.; Meng, F.; Suri, S.; Ding, W.; Huang, F.; Wu, N. Photoelectrochemical Performance Enhanced by a Nickel Oxide−Hematite *p*−*n* Junction Photoanode. *Chem. Commun.* **2012**, *48*, 8213−8215.

DOI: 10.1021/acsami.5b02271
ACS Appl. Mater. Interfaces 2015, 7, 13905−13914